Using the Microwave Polarization Data to Evaluate Ice Crystal Properties Simulations

Xiping Zeng[1,2], Gail Skofronick-Jackson[2], Lin Tian[2,3], Amber E. Emory[2], Williams S. Olson[2,4], Rachael A. Kroodsma[5,6]

[1] Atmospheric Modeling Branch, US Army Research Laboratory, Adelphi, Maryland 20783

[2] Mesoscale Atmospheric Processes Laboratory, NASA Goddard Space Flight Center, Greenbelt, Maryland 20771

[3] Goddard Earth Sciences Technology and Research, Morgan State University, Baltimore, Maryland 21251

[4] Joint Center for Earth Systems Technology, Maryland of University, Baltimore County, Baltimore, Maryland 21250

[5] Earth System Science Interdisciplinary Center, University of Maryland, College Park, Maryland 20742

[6] Precipitation Processing System, NASA Goddard Space Flight Center, Greenbelt, Maryland 20771

Submitted to *the Journal of the Atmospheric Sciences*

August 29, 2017

Corresponding author address: Dr. Xiping Zeng, RDRL-CIE-M, U.S. Army Research Laboratory, Adelphi, MD 20783. Email: xiping.zeng.civ@mail.mil.

Abstract

Two NASA microwave radiometers, the satellite-borne GPM (Global Precipitation Measurement) Microwave Imager (GMI) and the aircraft-borne CoSMIR (the Conical Scanning Millimeter-wave Imaging Radiometer), measure vertically- and horizontally-polarized microwaves emitted by cloud particles and the Earth below, providing unique information on ice crystal properties in clouds. Their data reveal that non-spherical ice crystals are common and they fall in a preferred horizontally aligned orientation in convective and optically thick clouds especially near cloud top.

A bin (particle-size-resolving) microphysical model with an ice crystal shape representation is developed to simulate the evolution of ice crystal properties (i.e., size, shape and orientation), where the radiation effect on microphysics (REM) is taken into account. Since REM represents the effect of all (e.g., both infrared and solar) radiation on ice crystal temperature, it relies upon the ice crystal proprieties that determine how an ice crystal receives radiation. Definitely, REM is different from the radiative effects that cause sensitivity at the microwave frequencies in the GPM and CoSMIR observations.

Model results show that horizontally-oriented ice crystals grow faster than vertically-oriented (or spherical) ones due to REM. When both horizontally- and vertically-oriented ice crystals coexist in an air parcel, the model results show that the former grow by vapor deposition whereas the latter shrink by sublimation and disappear eventually. These modeling results are supported by the GMI data and the CoSMIR observations from MC3E (Midlatitude Continental Convective Clouds Experiment) and OLYMPEX (Olympic Mountains Experiment) on the prevalence of horizontally-oriented ice crystals. Moreover, the REM-induced precipitation explains the CloudSat observations of rare thin

clouds in the tropical mid-troposphere as well as the common diamond dust in the high latitudes.

1. Introduction

Ice clouds in the upper troposphere play a crucial role in the Earth's radiation balance due to their widespread and long lifetime (e.g., Webster and Stephens 1980, Hartmann et al. 1984, Harrison et al. 1993, Zeng et al. 2009). However, they are not represented well in current weather and climate models (e.g., Zhang et al. 2005, Klein et al. 2009, Jiang et al. 2012). Field campaign and laboratory observations show that the ice crystals growing from the vapor phase are usually non-spherical (Pruppacher and Klett 1997). Since ice crystal shape is important in radiation computation (e.g., Liu et al. 1998, Yang et al. 2005), how to better model and observe ice crystal properties (i.e., size, shape and orientation) is imperative to parameterize non-spherical ice crystals in climate models.

Since aircraft penetration observations of ice crystals are expensive and limited over few geographic regions, the remote sensing of ice crystal shape is becoming important (e.g., Sassen 1974, Intrieri et al. 2002, Noel and Chepfer 2010, Neely et al. 2013, Skofronick-Jackson et al. 2015). In 2014, the GPM (Global Precipitation Measurement) satellite was launched (Hou et al. 2014, Skofronick-Jackson et al. 2015), where GMI (the GPM Microwave Imager) measures the intensity of radiation (via brightness temperature) at high frequencies (e.g., 166 and 183 GHz) that were added to GMI specifically for observing ice, snow and graupel properties. GMI's microwave polarization data (e.g., 166V, 166H) can be used to analyze the distribution of ice crystal shape (Skofronick-Jackson et al. 2008, Emory et al. 2013, Gong and Wu 2017). To support the analysis of satellite data, CoSMIR (the Conical Scanning Millimeter-wave Imaging Radiometer) that functions similarly as GMI was flown on the NASA ER-2 and DC-8 aircrafts during the Midlatitude Continental Convective Clouds Experiment (MC3E) and Olympic Mountains

Experiment (OLYMPEX) for clouds and precipitation observations (Jensen et al. 2016, Houze Jr. et al. 2017). In this study, the polarization data of GMI and CoSMIR are analyzed for the distribution of ice crystal properties. To better understand the GMI and CoSMIR data on ice crystal properties, a bin microphysical model that explicitly considers crystal shape and the radiation effect on microphysics (REM) (e.g., Zeng 2008) is developed to replicate the evolution of ice crystals in shape and size, where REM is different from the radiative effects that cause sensitivity at the microwave frequencies in the GPM and CoSMIR observations.

The study was introduced in the 2016 PMM (Precipitation Measurement Mission) meeting briefly (Zeng et al. 2016) and completely herein by five sections. In Sec. 2, REM is incorporated into a numerical model for ice crystal shape simulations. In Sec. 3, numerical simulations are carried out to show how REM impacts ice crystal size and shape. In Sec. 4, model results are compared with GMI and CoSMIR data for model evaluation. Sec. 5 gives a summary. Except for special illustrations, all symbols are defined in the Appendix.

2. Representing the radiation effect on microphysics (REM)

a. The REM processes

REM consists of a series of processes. That is, radiation impacts the surface temperature of cloud particles that in turn affects the saturation water vapor pressure around the particles and eventually alters the diffusional growth rate of the particles (e.g., Hall and Pruppacher 1976, Roach 1976, Stephens 1983, Wu et al. 2000, Zeng 2008). REM exists in two common weather phenomena: dew and frost in unsaturated air (e.g., Koeppe and De Long 1958). It also exists in ice clouds as a precipitation mechanism

(Zeng 2008). This section shows how to incorporate REM into a bin model for ice crystal shape simulations, beginning with REM for a single ice crystal.

For a single ice crystal of mass m, its microscopic radiative ratio η is defined as the ratio of the infrared flux incident on ice crystal surface to the radiative flux emitted by the ice crystal as a blackbody at its environmental air temperature (Zeng 2008). Hence, η *approximately represents the ratio of the inward radiative flux to the outward one at crystal surface*. When $\eta = 1$, the ice crystal grows just as predicted by the classic theory of cloud physics without REM (Fuchs 1959, Rogers and Yau 1989).

If the atmosphere were a black body, $\eta \approx 1$. In fact, the atmosphere has quasi-transparent regions within the radiative spectrum (or atmospheric windows) and thus is not a blackbody (e.g., Stephens 1983). Hence, η usually deviates from one. As a result, radiation alters the ice crystal temperature and subsequently the saturation water vapor pressure around the crystal. An analytical expression of the ice crystal growth rate is derived as a function of η (Zeng 2008).

Figure 1 illustrates the saturation water vapor pressure E_i against ice crystal size when $\eta > 1$ and $\eta < 1$, respectively. The dependence of E_i (or ice crystal temperature) on crystal size originates in the different sensitivities of the radiative and conductive energy fluxes at crystal surface to ice crystal size. For a spherical ice crystal of radius r, for example, the radiative fluxes at crystal surface are directly proportional to r^2 (or crystal surface area), whereas the conductive energy flux is proportional to r (or crystal size) only.

When $\eta < 1$, E_i decreases with increasing crystal size. Hence, an ice crystal can grow in an unsaturated environment, reaching a size of millimeters (see Sec. 3a for modeling).

This growth mechanism resembles the formation of a dew-drop (or frost) in an unsaturated environment if the dew-drop and its supporter (e.g., wide grass leaf) are treated together for a heat balance.

Consider REM for two adjacent ice crystals shown in Fig. 1. When $\eta > 1$ (red lines), the larger crystal has a higher temperature and subsequently larger saturation water vapor pressure around it. As a result, the larger crystal sublimates with the resulting water vapor being deposited onto the smaller crystal. In contrast, when $\eta < 1$ (green lines), the smaller crystal has a higher temperature and subsequently larger saturation water vapor pressure around it. Therefore, the smaller crystal sublimates with the resulting water vapor being deposited onto the larger particle, which serves as a precipitation mechanism (Zeng 2008).

Consider multiple ice crystals that coexist in an air parcel. They compete for water vapor available and REM alters their competition for water vapor. As a result, REM brings about a nonlinear evolution of ice crystal spectrum. Zeng (2008) developed a bin (or particle-size-resolving) model to simulate how REM impacts ice crystal size for a given ice crystal shape. In this paper, the model is extended to simulate how REM impacts both size and shapes of ice crystals.

b. Representing ice crystal shapes

Consider an air parcel with ice crystals that moves with vertical velocity *w*. Its tendency of the relative humidity with respect to ice H_i, based on the conservation of energy and water, is derived as (Rogers and Yau 1989, Zeng 2008)

$$\frac{dH_i}{dt} = Q_1(T)w - Q_2(T)\sum_{j,k}\frac{dm_{jk}}{dt} \tag{1}$$

where T is air temperature, m_{jk} (j=1, 2, …) denotes the mass of differently sized ice crystals for a given crystal shape k, and

$$Q_1(T) = \frac{1}{T}\left[\frac{L_s g}{R_v C_p T} - \frac{g}{R_d}\right] \tag{2}$$

$$Q_2(T) = \rho_a\left[\frac{R_v T}{E_i(T)} + \frac{R_d L_s^2}{p R_v C_p T}\right]. \tag{3}$$

All ice crystals are classified into five shapes (or k =1, … , 5): (1) a sphere of radius r and surface area $S = 4\pi r^2$ for graupel, (2) a prolate spheroid of semi-major and minor axis lengths a and b for column-like crystals, whose surface area is

$$S = 2\pi b\left(b + \frac{a^2}{\sqrt{a^2 - b^2}}\arcsin\frac{\sqrt{a^2 - b^2}}{a}\right), \tag{4}$$

(3) an oblate spheroid of semi-major and minor axis lengths a and b for plate-like crystals, for which

$$S = 2\pi a\left(a + \frac{b^2}{\sqrt{a^2 - b^2}}\ln\frac{\sqrt{a^2 - b^2} + a}{b}\right), \tag{5}$$

(4) a prolate spheroid for bullet-shaped crystals, and (5) a sphere for rosette crystals that consist of bullets. All of the crystal shapes have their own formulas of ice crystal mass, terminal velocity, dimensional relationship and ventilation factors against crystal size. The formulas are empirically obtained from field observations (e.g., Auer and Veal 1970; Heymsfield 1972; Heymsfield and Iaquinta 2000; see Zeng 2008 for computational details).

c. Computing η

The growth rate of an ice crystal, or dm/dt in Eq. (1), is derived as a function of η (Zeng 2008), which is rewritten, after some algebraic operations, as

$$\frac{dm}{dt}=\frac{4\pi C(H_i-1)}{H_{ic}A+B}+\frac{S\varepsilon_0\sigma T^3}{KF_\alpha f_Q(H_{ic}A+B)}\left(\frac{L_s}{R_vT}-1\right)\left(1-\varepsilon_r\eta-\frac{F_s}{\varepsilon_0\sigma T^4}\right) \qquad (6)$$

where σ is the Stefan-Boltzmann constant, C the stationary diffusion shape factor that accounts for the influence of crystal shape on the water vapor field around a crystal (for a spherical crystal of radius r, $C = r$),

$$A=\frac{L_s}{F_\alpha f_Q KT}\left(\frac{L_s}{R_vT}-1\right) \qquad (7)$$

$$B=\frac{R_vT}{F_\beta f_m DE_i(T)} \qquad (8)$$

and

$$H_{ic}=1-\left(\frac{L_s}{R_vT}-1\right)\left(1-\varepsilon_r\eta-\frac{F_s}{\varepsilon_0\sigma T^4}\right)\frac{S\varepsilon_0\sigma T^3}{4\pi CKF_\alpha f_Q} \qquad (9)$$

(see the Appendix for the other symbol definitions).

The ratio η in (6) is computed as follows. Let F^+ and F^- represent the upward and downward fluxes of infrared radiation in the atmosphere, respectively, and define the macroscopic radiative ratio of an air parcel as (Zeng 2008)

$$\eta_z=\frac{F^++F^-}{2\sigma T^4}. \qquad (10)$$

Once atmospheric variables are given, η_z is obtained easily by using a two-stream radiation package to calculate F^+ and F^- (e.g., Fu and Liou 1992, Chou *et al*. 1995).

The ratio η_z is used to determine η, which is illustrated with Fig. 2. Consider an ice crystal that receives the upward radiation (F^+), downward radiation (F^-) and horizontal radiation ($\approx\sigma T^4$), where σT^4 represents the blackbody irradiance at air temperature T.

Since the atmosphere is not a blackbody, the upward infrared flux F^+ and the downward one F^- usually deviate from the horizontal one (or σT^4). Their contribution to an ice crystal is approximated with (F^++F^-) times the maximum horizontal cross section area of the crystal, which depends on the shape and orientation of the crystal.

A horizontally-oriented plate-like ice crystal is discussed first. It is mimicked by an oblate spheroid of semi-major and minor axis lengths *a* and *b*. Since its maximum horizontal cross section area is πa^2, the spheroid receives the upward and downward infrared fluxes $\pi a^2 F^+$ and $\pi a^2 F^-$, respectively, whereas the rest surface area of the crystal (or S-$2\pi a^2$) receives the horizontal infrared flux σT^4 from the crystal environment. Hence, the total radiative flux received equals $\sigma T^4(S-2\pi a^2) + \pi a^2(F^+ + F^-)$. Substituting (10) into the total radiative flux to eliminate $F^+ + F^-$ and then dividing the resulting expression with $\sigma T^4 S$ yields the expression of η. That is,

$$\eta - 1 = \frac{2\pi a^2}{S}(\eta_z - 1)\,, \tag{11a}$$

where S is calculated with Eq. (5). When $b << a$, $\eta \approx \eta_z$.

A vertically-oriented plate-like crystal is still mimicked with an oblate spheroid of semi-major and minor axis lengths *a* and *b*, but its maximum horizontal cross section area becomes πab. Following the same procedure to (11a), η for a vertically-oriented plate-like ice crystal is obtained, i.e.

$$\eta - 1 = \frac{2\pi ab}{S}(\eta_z - 1)\,. \tag{11b}$$

Consider a bullet-shaped crystal similarly. A horizontally (or vertically) oriented bullet-shaped crystal is mimicked by a prolate spheroid of semi-major and minor axis lengths *a* and *b* that has a maximum horizontal cross section area of πab (or πb^2). Thus,

$$\eta - 1 = \frac{2\pi ab}{S}(\eta_z - 1) \quad (12a)$$

$$\eta - 1 = \frac{2\pi b^2}{S}(\eta_z - 1) \quad (12b)$$

are obtained for horizontally- and vertically-oriented bullet-shape crystals, respectively, where S is from Eq. (4).

Furthermore, the connection of η_z to η for a spherical ice crystal is obtained similarly as

$$\eta - 1 = \frac{1}{2}(\eta_z - 1)\,. \quad (13)$$

Equations (11)-(13) can be summarized into a unifying expression or

$$\eta - 1 = \alpha(\eta_z - 1)\,, \quad (14)$$

where the coefficient α varies with crystal size, shape and orientation and falls between zero and one. For a vertically oriented ice crystal with extremely long axis ($b << a$), $\alpha = 0$ and thus $\eta = 1$. For a spherical crystal, $\alpha = 0.5$. For a horizontally oriented crystal with extremely long axis ($b << a$), $\alpha = 1$ and thus $\eta = \eta_z$.

Although η_z and η are connected via Eq. (14), they have different applications. Since the macroscopic ratio η_z is independent of crystal properties, it can be treated as a property (i.e., the asymmetry between horizontal and vertical irradiances) of an air parcel and therefore can be used as a variable in cloud or climate models. In contrast, the microscopic ratio η varies with ice crystal size, shape and orientation, and thus is suitable to discuss the growth rate of individual ice crystals (e.g., Fig. 1). Since (η_z - 1) has the same sign as (η - 1), η_z usually takes the place of η in discussing REM except for specification.

3. Numerical simulations of ice crystal properties

The parcel model in Sec. 2b is used to simulate how REM impacts the ice crystals in an air parcel of η_z = 0.5, where η_z = 0.5 corresponds to a cloud position with $F^- \approx 0$ (or near cloud top) approximately. In the present paper, the effect of solar radiation on crystals (e.g., Stephens 1983, Zeng 2008) is not discussed explicitly (or F_s=0 is set). Instead, it can be discussed implicitly by tuning the magnitude of η_z to take account of F_s. Since there is a net radiative cooling (or net η_z <1) near cloud top even in daytime (e.g., Liou 1980) and the GMI observations at 166 GHz showed that the solar effect is about one third of the infrared one (Gong et al. 2017), the present simulations with η_z <1 are carried out to understand REM qualitatively.

Six numerical experiments are carried out to test the sensitivity of ice crystal properties to REM (see Table 1 for the experiment summary). Except for specification, all of the experiments are set up as follows. All model variables are represented in double precision. Their prognostic equations are integrated with 2048 bins, using a time step of 0.2 s with a second-order accuracy. The initial relative humidity with respect to ice is set to 100%. The air temperature T = -30°C, pressure p = 300 hPa, and η_z = 0.5. In addition, the vertical velocity w = 0.

a. Contribution of REM to snow formation

Diamond dust (or clear-sky precipitation) is common in the arctic regions especially in winter (e.g., Liu et al. 2012, Bennartz et al. 2013, Shupe et al. 2013). It involves neither riming nor aggregation. Since it is "simple" and η_z < 1 in the arctic regions (see Sec. 4a), it is simulated here using the bin model to show how REM impacts the shape and orientation of ice crystals.

The default experiment Ph addresses the evolution of horizontally-oriented plate crystals. Its initial ice crystal spectrum, shown by the thick line in Fig. 3, has an ice crystal concentration of 0.5 cm^{-3} and an ice water content (IWC) of 3.6×10^{-4} g m^{-3}. If η_z = 1, the ice crystals would maintain their initial spectrum without snow formation. However, if η_z = 0.5, the situation changes. Figure 3 displays the modeled broadening of ice crystal spectrum with η_z = 0.5, showing that precipitating particles form in a few hours. The spectral discontinuity near 200 μm coincides with the emergence of dendritic extensions at that size.

The average (half) crystal size for a given shape k is defined as

$$\bar{a}_k = \sum_j aM_{jk} \Big/ \sum_j M_{jk} ,$$

where M_{jk} represents the mass of ice crystals in a bin of j and k. Figure 4 displays the average crystal size, IWC and H_i against time in Ph, showing that the modeled process resembles the frost formation. When the average crystal size increases with time, REM leads to the decrease in the average crystal temperature and the saturation water vapor pressure around the crystals. As a result, water vapor deposits on ice crystals and the environmental relative humidity (or H_i) decreases with time.

An interesting phenomenon in Fig. 4 is the dramatic increase (or decrease) in ice crystal size (or relative humidity) from hour 5.5 to 6.5. This dramatic change originates in the crystal dimensional relationship as well as the ventilation factors for mass transfer and thermal diffusion. That is, the ratio of crystal length to thickness and the ventilation factors increase with ice crystal size (e.g., Auer and Veal 1970; Pruppacher and Klett 1997), which brings about the dramatic increase of ice crystal size after the ice crystal size is longer than 1 mm. The dramatic change explains the formation of diamond dust in the dry arctic regions (e.g., Shupe et al. 2013).

b. Selection of ice crystal orientations

Two experiments PhPv and ChCv are carried out to test the selection of ice crystal orientations due to REM. The PhPv simulates plate crystals with two orientations. It takes the same setup as Ph except that half of the crystals are horizontally oriented and the other half are vertically oriented. Figure 5 displays the modeled spectra of vertically- and horizontally-oriented ice crystals. The horizontally-oriented ice crystals, just like those in Ph, grow to form precipitating particles in a few hours. In contrast, the vertically-oriented crystals shrink due to sublimation and disappear eventually (Fig. 5a), because the vertically-oriented ones have higher temperature than the horizontally-oriented ones when η_z <1 (see Fig. 2).

The ChCv experiment simulates column crystals with two orientations. It takes the same setup as PhPv except for column crystals. Its modeled spectra are displayed in Fig. 6, showing that horizontally-oriented crystals grow faster than vertically-oriented ones. The comparison of Figs. 5 and 6 indicates that plate crystals grow faster than column ones. In spite of their difference in growth rate, both experiments show that REM favors horizontally-oriented ice crystals, which explains the observed prevalence of horizontally-oriented ice crystals (e.g., Neely et al. 2013, Shupe et al. 2013; see Sec. 4c for a simulation evaluation).

c. Selection of ice crystal shapes

Ice crystal habit (or shape) varies with temperature and supersaturation (e.g., Magono and Lee 1966, Murray et al. 2015, see Pruppacher and Klett 1997 for review). Since

REM impacts crystal temperature and supersaturation via crystal size and shape, REM can affect ice crystal shape by selecting fast-growing crystals to survive. In this subsection, two experiments PhS and PhCh are carried out to test how REM selects crystal shapes.

Experiment PhS simulates spherical solid ice crystals (or graupels if they fall into the parcel) mixed with horizontally-oriented plate ones. It takes the same setup as PhPv except that spherical crystals take the place of the vertically-oriented plate ones. Just like those in PhPv (or Fig. 5), the horizontally-oriented plate crystals grow to form precipitation while the spherical ones disappear. Figure 7 displays the average radius of spherical ice crystals against time. The average radius increases with time first and then decreases dramatically after the plate crystals reach a size of ~ 200 μm with the emergence of dendritic extensions. These results indicate that horizontally-oriented plate crystals are selected to survive by REM when they coexist with spherical ones in an air parcel, which partly explains that non-spherical ice crystals are common in cirrus clouds.

Experiment PhCh simulates plate crystals mixed with column ones by the same number concentration, where all of the ice crystals are horizontally oriented. The experiment is set up as PhPv except that the horizontally-oriented column crystals take the place of the vertically-oriented plate ones. Just like those in PhPv, the horizontally-oriented plate crystals instead of column ones are selected to survive by REM, because plate crystals grow faster than column ones (figure omitted).

d. Effect of vertical velocity

Vertical velocity impacts parcel relative humidity that in turn affects ice crystal growth. In this section, Exp. PhPvW is carried out to test whether vertical velocity alters the selection of crystal orientations. The experiment is set up as PhPv except for a vertical velocity of w = 1 cm s^{-1}. Figure 8 displays the modeled evolution of the horizontally-oriented plate crystals, and Fig. 9 displays the average crystal sizes of horizontally- and vertically-oriented crystals. The horizontally-oriented ice crystals, just like those in PhPv, grow to form precipitation in a few hours whereas the vertically-oriented ones disappear in 1.5 hour, showing that vertical velocity does not alter the selection of crystal orientations.

Figure 9 also displays the time series of IWC and crystal size in both PhPvW and PhPv, showing that vertical velocity increases IWC significantly. Interestingly, the average sizes of ice crystals in PhPvW and PhPv are close to each other, which exhibits the insensitivity of ice crystal spectrum broadening to vertical velocity. These different sensitivities of IWC and crystal size to vertical velocity suggest that REM, instead of vertical velocity, is the major contributor to the crystal spectrum broadening. The sensitivities also suggest that REM can be used to overcome the modeling problem of too narrow crystal spectrum that exists in the current cirrus models (Starr and Quante 2002).

4. Comparison to GMI and CoSMIR data

Since horizontally-oriented ice crystals are favored in an environment of $\eta_z < 1$ (see Table 1 for the experiment summary), their geographical distribution depends on the distribution of $\eta_z < 1$. In this section, the geographical distribution of η_z is analyzed first and then compared to that of GMI and CoSMIR 166V and 166H brightness temperature differences as an evaluation of ice crystal model simulations.

a. Meridional variation of η_z

The radiative ratio η_z varies greatly with atmospheric temperature, water vapor, sea/land surface temperature and clouds. However, its distribution for clear sky is relatively simple and thus provides a first-order approximation to understand thin cirrus clouds (including diamond dust)[1].

The ratio η_z in clear sky is computed, using Eq. (10) and the Goddard radiation package with the data of mean atmospheric states in the low, middle and high latitudes (Chou *et al*. 1995). Figure 10 displays the vertical profiles of η_z in winter and summer in the high latitudes, showing that η_z is less than one in both seasons. Moreover, η_z in winter is much smaller than that in summer, because the underlying surface temperature in winter is much lower than that in summer. For comparison, Fig. 11 displays the vertical profiles of η_z in the Tropics and mid-latitudes, showing that $\eta_z < 1$ in the lower and middle troposphere but $\eta_z > 1$ in the upper troposphere in the Tropics and middle latitudes. Generally speaking, η_z decreases with increasing latitude, from $\eta_z > 1$ in the upper troposphere in the Tropics to $\eta_z < 1$ in the Arctic. This meridional variation of η_z is clear in physics, because the underlying surface temperature and subsequently the upward radiative flux F^+ decrease with increasing latitude.

Furthermore, clouds change the vertical profile of η_z significantly. For thick clouds, their lower part blocks the upwelling infrared radiation from the underlying surface and consequently $\eta_z < 1$ near and above cloud top, no matter how high the underlying surface

[1] Suppose that there is only one ice crystal in clear sky. Although the crystal contributes little to the atmospheric radiation transfer, the atmospheric radiation impacts the crystal temperature effectively. Hence, the growth of the crystal can be understood with η_z in clear sky. Similarly, if a thin cloud contributes little to the atmospheric radiation transfer, its crystal growth can be understood approximately with η_z in clear sky.

temperature is (Zeng 2008). Since the model results show that horizontally-oriented ice crystals are favored radiatively with $\eta_z < 1$, it is predicted that the frequency of occurrence for horizontally-oriented ice crystals is high near the top of thick clouds and the frequency in thin clouds increases with latitude. Such prediction on ice crystal orientation is evaluated with observational data next.

b. CoSMIR data

Passive microwave (PMW) radiometers such as CoSMIR and GMI measure the upwelling radiances emitted by the atmosphere, clouds, precipitation and the Earth below (e.g., Skofronick-Jackson and Johnson 2011). Their data can be used to retrieve hydrometeor particle information and rain rates (e.g., Kummerow 1993, Olson et al. 2001a, Liu 2004). Since ice crystals in the atmosphere scatter Earth's upwelling microwave radiation especially at high frequencies (> 85 GHz), the amount of microwaves scattered and thus received by PMW radiometers depend on ice crystals aloft (Skofronick-Jackson et al. 2015). If the ice crystals are non-spherical (e.g., plate-like) and oriented with respect to the PMW viewing angle, the microwaves received by PMW radiometers become polarized (e.g., Roberti and Kummerow 1999, Adams et al. 2008). Hence, the difference in radiance between horizontally- and vertically-polarized channels, especially at high frequencies (e.g., 166 GHz), should be able to measure the general orientation of ice crystals. Generally speaking, when the GMI brightness temperature (T_b) at 166 GHz for vertically polarized microwaves is higher than that for horizontally polarized microwaves, there are horizontally-oriented ice crystals aloft (e.g., Roberti and Kummerow 1999, Adams et al. 2008, Defer et al. 2014).

CoSMIR and GMI are both PMW radiometers with high frequencies at 166 GHz and operating with conical scans (thus at an approximate 53.6 degree viewing angle to the hydrometeors in the cloud) (Wang et al. 2007, 2008; Draper et al. 2015). The CoSMIR is loaded on the NASA ER-2 aircraft to observe clouds downwards with a footprint of 2.5×4.3 km^2. Its data from MC3E are analyzed next, providing an analysis procedure for GMI data.

MC3E was a field campaign in south-central Oklahoma, conducted during April through June 2011 and jointly led by the NASA GPM Mission and the U.S. Department of Energy's ARM (Atmospheric Radiation Measurement) program (Jensen et al. 2016). In the campaign, CoSMIR and several radars [including the HIWRAP (high-altitude imaging wind and rain airborne profile) radar] were in the high-altitude ER-2 aircraft to measure upwelling microwaves and hydrometeors (Heymsfield et al. 2013).

CoSMIR data from MC3E are analyzed here to show the ice crystal orientation in a mesoscale convective system (MCS). Figure 12 displays the horizontal cross-section of radar reflectivities at 10 cm wavelength (or 3 GHz frequency) at an altitude of 3 km at 2234 UTC May 23 from the ground-based NPOL (NASA S-Band Dual-Polarimetric Radar) located at 36.5N and 97.2W. The figure also displays the ER-2 flight track from 2223 to 2241 UTC, 23 May 2011. This flight period is chosen for analysis because its observations cover both deep convection and anvil clouds.

The HIWRAP radar and CoSMIR observations in the flight period are analyzed. Figure 13 displays the vertical cross section of Ku-band (2.8 cm wavelength) reflectivity (dBZ) from the HIWRAP radar that scans downwards, showing that there is deep convection, stratiform clouds and anvil clouds during the flight period. The figure also displays the difference in the brightness temperature T_b at 165.5 GHz between vertical and horizontal polarization (referred to here as polarization difference). Since CoSMIR scans at an off-nadir-angle of 53.6 degrees, a distance shift of 5.5 km is applied to the CoSMIR data so that the CoSMIR data in the figure correspond to the radar data below.

Figure 13 shows that the brightness temperature T_b at 165.5 GHz for vertical polarization is much higher than that for horizontal polarizations over stratiform clouds and anvil clouds, whereas T_b for vertical polarization is slightly higher than that for horizontal one over deep convection (Heymsfield and Fulton 1994, Gong and Wu 2017). Such difference in T_b suggests that a large fraction of ice crystals in non-convective regions are horizontally oriented but only a small fraction of ones in deep convection are horizontally oriented. Indeed, in deep convection particles are experiencing updrafts that (1) cause them to rotate almost randomly with no preferred orientation via turbulence and (2) detrain them near cloud top so that REM has insufficient time to select horizontally-oriented crystals.

c. Comparison of CoSMIR *and GMI data*

The satellite-borne GMI functions similarly as the aircraft-borne CoSMIR. Its footprint at 166 GHz is approximately 4.1×6.3 km^2 that is larger than that of CoSMIR (i.e., 2.5×4.3 km^2 in MC3E and 1.3×1.9 km^2 in OLYMPEX)[2]. In this subsection, the GMI and CoSMIR data are compared over the OLYMPEX region, showing that GMI and CoSMIR measured the polarization difference consistently.

[2] The footprint of CoSMIR depends on not only the CoSMIR off-nadir angle but also the height of CoSMIR (or aircraft). To better match the GMI off-nadir angle, CoSMIR on the DC-8 aircraft took an off-nadir angle of 49 degrees in OLYMPEX, bringing about a footprint of 1.3×1.9 km^2 for the conical scan.

OLYMPEX is a field campaign to observe precipitation over the Olympic Mountains near Seattle from November 2015 through February 2016 (Houze Jr. et al. 2017). Different from MC3E, OLYMPEX addressed cloud systems that were mostly stratiform and also emphasized GPM core overpasses, providing unique data to compare the observations of GMI and CoSMIR.

In the campaign, CoSMIR was loaded on the NASA DC-8 aircraft to measure upwelling microwaves with nine channels, two of which are at 165.5 GHz with both vertical and horizontal polarization. The two cloud systems observed on December 3 and 5 are selected for analysis when the GPM core satellite (with GMI) and DC-8 (with CoSMIR) flew over the campaign region at the same time. Specifically, CoSMIR scanned from 14:33 to 16:59 UTC 3 December, between 46.49 and 49.59°N and between 121.89 and 126.26°W while GMI flew over the region at 15:22 UTC 3 December; and from 14:18 to 15:38 UTC 5 December, between 46.45 and 48.61°N and between 122.4 and 125.65°W while GMI flew over the region at 15:13 UTC 5 December 2015.

The data from CoSMIR and GMI over the CoSMIR scan regions are displayed in Fig. 14 for comparison, showing that the polarization difference over stratiform clouds is positive and becomes largest at horizontal polarization T_b of ~200K and smallest at ~270K. Such positive polarization difference is consistent with that over the stratiform clouds during MC3E.

Figure 14 also shows that the scattering of GMI polarization difference is narrower than that of CoSMIR. Such difference between GMI and CoSMIR data is attributed to their difference in footprint (or scan volume). In other words, the GMI data at 166 GHz represent the average of T_b over a larger area than those of CoSMIR. Although the GMI data are different from CoSMIR in scan volume, they still catch the same main characteristics of polarization difference as the CoSMIR data and hence are used to statistically analyze the polarization difference from GMI.

d. Statistics of GMI data

The statistical analysis of polarization difference is carried out using three-year data of GMI and CloudSat data (Stephens et al. 2002), which resembles the MC3E analysis in Sec. 4.b except that GMI and CloudSat replace CoSMIR and the HIWRAP radar, respectively. A GPM data product of 2B.CSATGPM compiles the coincident data of GPM and CloudSat while CloudSat flew over GPM data pixels. Its 3687 coincident datasets, which spans from 8 March 2014 to 4 December 2016, are used for statistical analysis.

One of the datasets is analyzed first as an example. Figure 15 displays the vertical cross-section of CloudSat radar reflectivity and the GMI polarization difference ΔT_b (=166V-166H) at 166 GHz along the same CloudSat track over the Amazon on 13 November 2014. The figure suggests that the polarization difference is positive over thick clouds but close to zero over thin cirrus clouds in the Tropics. Note that the polarization difference is close to 10K in stratiform cloud regions where it is expected that the ice particles are not subject to the turbulence in convective regions and thus can remain in a relatively fixed orientation. This nearly 10K difference was also true for the CoSMIR data.

The statistical analysis of GMI data supports the ΔT_b results obtained from the preceding cases. To show the sensitivity of ΔT_b to latitude, clouds and the underlying surface, atmospheric columns (or pixels) are classified into four thicknesses: deep-convective, thick, thin and extremely thin clouds (including diamond dust and clear-sky cases) when the maximum CloudSat radar reflectivity above 3 km is larger than 20 dBZ, between 5 and 20 dBZ, between -20 and 5 dBZ and less than -20 dBZ, respectively. The thicknesses are further distinguished by their underlying surface of sea and land. Finally, the thicknesses are divided into three geographical zones or latitudes lower than 25°, between 25 and 50° and higher than 50°.

The data of GMI and CloudSat are analyzed for the probability distribution function (PDF) of ΔT_b at 166 GHz in the Tropics first. Figure 16 displays the PDFs of tropical ΔT_b over four kinds of clouds. The PDFs over the thin (both continental and oceanic) clouds are close to those over the extremely thin clouds, indicating that the 166 GHz channel cannot sense the contribution of the thin clouds to ΔT_b. In other words, ΔT_b over the thin clouds comes mainly from the underlying surface (Adams et al. 2008) and thus is treated as the background here for brevity.

Figure 16 also shows that the ΔT_b over the thick clouds is significantly larger than that over the thin clouds (or background distribution), exhibiting a positive contribution of thick clouds to ΔT_b. Specifically, the thick clouds bring about an additional ΔT_b increase of ~6K in the Tropics. Such positive contribution of thick clouds to ΔT_b indicates that thick clouds prefer a horizontally aligned orientation of ice crystals near cloud top, which is consistent with the distribution of $\eta_z < 1$ near cloud top (Zeng 2008).

Deep convective clouds, as shown in Fig. 16, contribute positively to ΔT_b too, but less than the thick clouds, which supports the case analyses in Fig. 13. Interestingly, the PDF of ΔT_b over oceanic convective clouds exhibits two peaks at 1.5 and 5.5K, which can be attributed to two physical processes: the upward transport of randomly oriented (via turbulence) ice crystals to cloud top and the REM near cloud top, respectively.

To show the meridional variation of ΔT_b, Fig. 17 displays the PDFs of ΔT_b over the thick and the thin clouds (or background) in the low, middle and high latitudes. The figure clearly shows that thick clouds contribute positively to the 166 ΔT_b in all of the latitudes. Even though the difference in PDF looks smaller in the middle and high latitudes than that in the low ones, the horizontally oriented ice crystals in thick clouds may contribute the same to ΔT_b in the middle and high latitudes as those in the low ones, because the background ΔT_b increases with latitude (Fig. 17) and thus a large amount of spherical (or randomly oriented) hydrometeors in the lower part of thick clouds depolarize the upwelling background (polarized) microwaves in the middle and high latitudes (Adams et al. 2008). In short, the positive contribution of thick clouds to ΔT_b exists in all latitudes and has no obvious meridional tendency, which indicates that thick clouds prefer a horizontally aligned orientation of ice crystals near cloud top and is consistent with the distribution of $\eta_z < 1$ near cloud top (Zeng 2008).

e. CALIPSO data

Field campaign and other satellite observations complement the preceding evaluation of ice crystal properties modeling. The observations of ground-based CAPABL (the Cloud Aerosol Polarization and Backscatter Lidar) reveal a large frequency of horizontally-oriented ice crystals in arctic thin clouds (Neely et al. 2013, Shupe et al. 2013). Furthermore, the lidar and radar data of the CloudSat and Cloud-Aerosol Lidar and Infrared Pathfinder (CALIPSO) satellites show that diamond dust is common in the Arctic, especially in later winter and early spring (Liu et al. 2012). These observations are consistent with the geographical and seasonal distributions of $\eta_z < 1$ in the high latitudes (or Fig. 10).

The lidar polarization data of CALIPSO reveal the global distribution of horizontally oriented ice crystals in optically-thin clouds, showing that many horizontally oriented ice crystals exist in warm ice clouds (>-35°C) but few in cold ice clouds (<-35°C; e.g., Noel and Chepfer 2010, Zhou et al. 2012). Such sensitivity of oriented crystals to temperature can be explained by the vertical distribution of η_z in Fig. 11. In the Tropics and mid-latitudes, η_z <1 at altitude below 10 km (or temperature above ~ -35°C) and η_z >1 at altitude above 10 km (or temperature below ~ -35°C), indicating that REM can bring about many horizontally oriented ice crystals in warm ice clouds but few in cold ice clouds. In addition, the fraction of ice clouds containing oriented crystals increases with increasing latitude (Noel and Chepfer 2012), which can be attributed to the decrease in η_z with latitude with the aid of REM.

f. CloudSat data

The CloudSat observations of tropical clouds are consistent with the vertical distribution of η_z. Figure 18 displays the vertical profiles of thin and thick cloud fractions over land and sea in the Tropics (or latitudes lower than 25°). The fractions of thin and thick clouds are obtained by counting the pixels with radar reflectivity between -20 and 5 dBZ and between 5 and 20 dBZ first and then normalized by their total pixel numbers above 2 km, respectively, where 2 km is chosen to avoid surface contaminated data (e.g., Marchand et al. 2008).

In Fig. 18, the vertical distribution of thick clouds (with radar reflectivity between 5 and 20 dBZ) exhibits the trimodal characteristics of tropical convection (Johnson et al.

1999). Since the fraction of thick clouds can be used to measure the detrainment of convection approximately, the strong detrainments at ~7.5 km and below 2 km correspond to the modes of deep and shallow convection, respectively (e.g., Riehl and Malkus 1958), whereas the strong detrainment at ~4.5 km corresponds to the third mode of cumulus congestus (Johnson et al. 1999).

The vertical distribution of thick clouds cannot explain the distribution of thin clouds (with radar reflectivity between -20 and 5 dBZ) especially the maximum thin cloud fraction near 11.5 km, although thick clouds work as a water source of thin clouds. Instead, the REM-induced precipitation can explain the vertical distribution of thin clouds. Since $\eta_z < 1$ below ~ 10 km (see Fig. 11), the precipitation works as a water sink of thin clouds there, which explains the small fraction of thin clouds below ~ 10 km. In contrast, $\eta_z > 1$ above 10 km and thus there is no water sink like the REM-induced precipitation there, which explains the largest thin cloud fraction near 11.5 km even though the detrainment rate there is not large.

The thin cloud fraction decreases with decreasing height from ~ 10 to 5 km, which is attributed to the variation in REM-induced precipitation rate. For a given η_z (<1), the REM-induced precipitation forms faster at lower height (or higher temperature) because the timescale of REM decreases greatly with increasing temperature or decreasing height (Zeng 2008).

The thin cloud fraction reaches its minimum at ~ 5 km because the air temperature is 0°C there. REM induces precipitation effectively only for non-spherical ice crystals and no ice crystals exist in thin clouds below 5 km. Besides, REM cannot bring about raindrops at the expense of small droplets (Roach 1976; also see Fig. 7 for a simulation of spherical crystals). Hence, the lack of efficient precipitation formation below 5 km explains the minimum of thin cloud fraction at ~5 km.

In addition to the tropical observations, the satellite observations of arctic clouds are consistent with the distribution of η_z, too. The lidar and radar data of the CloudSat and CALIPSO satellites reveal a relatively high frequency of diamond dust in later winter and early spring (Liu et al. 2012), which corresponds to the smallest magnitude of η_z in the Arctic in winter (see Fig. 10). They also reveal a PDF peak of cloud top height between 7 and 9 km, which corresponds well to the maximum of η_z near 8.5 km (or 300 hPa) in Fig. 10. In summary, the distribution of η_z agrees well with the GMI observations of ice crystal orientation and the CloudSat/CALIPSO observations, indicating that REM plays an important role in the water cycle of the atmosphere.

5. Summary

Although REM plays an important role in the water cycle of the atmosphere, it has not been incorporated into the current cloud and climate models. In this paper, its effects are modeled against the data from satellites (GPM and CloudSat) and field campaigns (MC3E and OLYMPEX), which are summarized below.

- A bin microphysical model with REM is developed to simulate the evolution of ice crystal properties (i.e., size, shape and orientation). Its results show that horizontally-oriented ice crystals grow faster than vertically-oriented (or spherical) ones when $\eta_z < 1$. If ice crystals with different shapes and orientations coexist in an air parcel with $\eta_z < 1$, horizontally-oriented ones grow while vertically-oriented (or spherical) ones shrink and disappear eventually, bringing about a selection of horizontally-oriented ice crystals.

- The three-year data of GMI microwave polarization at 166 GHz reveal that horizontally oriented ice crystals are common in optically thick clouds in all latitudes especially near cloud top, supporting the model prediction of ice crystal shape because $\eta_z < 1$ near thick-cloud top.
- The CloudSat data show that the fraction of thin clouds in the middle troposphere is much smaller than that in the upper troposphere in the Tropics. Such vertical distribution of thin clouds is consistent with the model prediction, because the REM-induced precipitation (or $\eta_z < 1$ below 10 km) exists in tropical thin clouds in the middle troposphere but not in the upper troposphere (or $\eta_z > 1$ above 10 km). In addition, the different signs of η_z -1 below and above 10 km (or -35°C) explain the CALIPSO observations of many and few horizontally oriented ice crystals in warmer and colder thin ice clouds, respectively (e.g., Noel and Chepfer 2010, Zhou et al. 2012).
- In the arctic regions, $\eta_z < 1$ from the troposphere to stratosphere. The bin model simulations show that REM can bring about diamond dust (or clear-sky precipitation) even in a dry environment. The simulation results explain the high frequency of diamond dust and the prevalence of horizontally-oriented ice crystals in the arctic regions (e.g., Liu et al. 2012, Bennartz et al. 2013, Neely et al. 2013, Shupe et al. 2013). Such consistency in diamond dust between model and observations extends the GMI results into the arctic regions.
- The bin model simulations show that REM, instead of vertical velocity, broadens the ice crystal spectrum in cirrus clouds, which suggests that REM can be used to

overcome the modeling problem of too narrow crystal spectrum that exists in the current cirrus models (Starr and Quante 2002).

REM will have two practical applications: (1) incorporated into the retrieval algorithm of GMI high-frequencies data for better precipitation products and (2) into multi-dimensional cloud/climate models to better replicate clouds and precipitation in the water cycle of the atmosphere.

Acknowledgments: The authors are grateful to Dr. R. Kakar at NASA headquarters for his support of this research. They would like to thank Dr. Joe Turk for providing the coincident data of GMI and CloudSat. They thank Drs. Gerry Heymsfield and James Wang as well as HIWRAP and CoSMIR Engineer groups for data processing and engineer supports. Special thanks are extended to Drs. Yangang Liu and James L. Cogen for their kind suggestions.

This research was supported by the NASA Precipitation Measurement Mission (PMM) project under grant NNX16AE24G. It was also supported by the NASA CloudSat/CALIPSO project under grant NNX16AM06G. The NASA Center for Climate Simulation (NCCS) and NASA Advanced Supercomputing (NAS) Division provide the computer time used in this research.

Appendix List of Symbols

a/b : semi-major/minor axis length

C : stationary diffusion shape factor

C_p : specific heat of dry air

D : diffusivity of water vapor

e : partial pressure of water vapor

E_i : saturation vapor pressure over ice

f_m/f_Q : ventilation factor for mass transfer/thermal diffusion

F_s : solar flux absorbed by an ice crystal

F^+/F^- : upward/downward infrared flux

F_α/F_β : factor for the kinetic effect in heat/water vapor diffusion

g : acceleration due to gravity

$H_i=e/E_i$: relative humidity with respect to ice

H_{ic} : critical relative humidity, see (9)

K : coefficient of thermal conductivity of dry air

L_s : latent heat of sublimation

m : mass of an ice crystal

$M(\ln a)$: mass of ice crystals with semi-major axis length shorter than a

$N(a)$: number of ice crystals with semi-major axis length shorter than a

R_d/R_v : gas constant for dry air/water vapor

p : air pressure

r : radius of a sphere

S : surface area of an ice crystal

t : time

T : (air) temperature

T_b : brightness temperature

w : vertical velocity

ε_0 : bulk absorption efficiency of an ice crystal for blackbody radiation

ε_r : relative bulk absorption efficiency of an ice crystal for infrared radiation

σ : the Stefan-Boltzmann constant

η : microscope radiative ratio of individual ice crystals, see (11)-(13)

η_z : macroscope radiative ratio of an air parcel, see (10)

ρ_a/ρ_v : density of air/water vapor

Δt : time step for numerical integration

ΔT_b : difference in brightness temperature between vertically- and horizontally-polarized microwaves

References

Adams, I. S., P. Gaiser, *and* W. L. Jones *(*2008*)*, Simulation of the Stokes vector in inhomogeneous precipitation. *Radio Sci.*, **43**, *RS5006, doi:*10.1029/2007RS003744.

Auer, A. H., and D. L. Veal, 1970: The dimension of ice crystals in natural clouds. *J. Atmos. Sci.*, **27**, 919-926.

Bennartz, R., M. D. Shupe, D. D. Turner, V. P. Walden, K. Steffen, C. J. Cox, M. S. Kulie, N. B. Miller, and C. Pettersen, 2013: July 2012 Greenland melt extent enhanced by low-level liquid clouds. *Nature*, **496**, 83-86, doi:10.1038/nature12002.

Chou, M.-D., W. Ridgway, and M.-H. Yan, 1995: Parameterizations for water vapor IR radiative transfer in both the middle and lower atmosphere. *J. Atmos. Sci.*, **52**, 1159-1167.

Draper, D. W., D. A. Newell, F. J. Wentz, S. Krimchansky and G. Skofronick-Jackson, 2015: The Global Precipitation Measurement (GPM) Microwave Imager (GMI): Instrument Overview and Early On-orbit Performance. IEEE Journal of Selected Topics in Applied Earth Observations and Remote Sensing, **8**, 3452-3462, doi:10.1109/JSTARS.2015.2403303.

Emory, A., D. Short, L. Tian, W. Petersen and G. Heymsfield, 2013: Observations of Deep Convection during MC3E using Ground-Based Radars and Airborne Radiometers and Implementation in GPM DPR Off-Nadir Simulations. *AMS 36th Conference on Radar Meteorology*, Breckenridge, Colorado.

Fu, Q., and K.-N. Liou, 1992: On the correlated k-distribution method for radiative transfer in nonhomogeneous atmospheres. *J. Atmos. Sci.*, **49**, 2153-2170.

Fuchs, N. A., 1959: *Evaporation and droplet growth in gaseous media*. Pergamon Press, 72 pp.

Gong, J. and D. L. Wu, 2017: Microphysical properties of frozen particles inferred from Global Precipitation Measurement (GPM) Microwave Imager (GMI) polarimetric measurements. *Atmos. Chem. Phys.*, **17**, 1–17, 2017, doi:10.5194/acp-17-1-2017.

Gong, J., X. Zeng, D. L. Wu and X. Li, 2017: Diurnal variation of tropical ice cloud microphysics: Evidence from Global Precipitation Measurement Microwave Imager (GPM-GMI) polarimetric measurements. *J. Geophys. Lett*. (submitted).

Hall, W. D., and H. R. Pruppacher, 1976: The survival of ice particles falling from cirrus clouds in subsaturated air. *J. Atmos. Sci.*, **33**, 1995-2006.

Harrison, E. F., P. Minnis, B. R. Barkstrom, and G. G. Gibson, 1993: Radiation budget at the top of the atmosphere. *Atlas of Satellite Observations Related to Global Change*, R. J. Gurney, J. L. Foster, and C. L. Parkinson, Eds., Cambridge University Press, 19-38.

Hartmann, D. L., H. H. Hendon, and R. A. Houze, Jr., 1984: Some implications of the mesoscale circulations in tropical cloud clusters for large-scale dynamics and climate. *J. Atmos. Sci.*, **41**, 113-121.

Heymsfield, A., 1972: Ice crystal terminal velocities. *J. Atmos. Sci.*, **29**, 1348-1357.

Heymsfield, A. J., and J. Iaquinta, 2000: Cirris crystal terminal velocities. *J. Atmos. Sci.*, **57**, 916-938.

Heymsfield, G. M., and R. Fulton, 1994: Passive microwave and infrared structure of mesoscale convective systems. *Meteor. Atmos. Phys.*, **54**, 123-139.

Heymsfield, G. M., L. Tian, L. Li, M. McLinden, and J. I. Cervantes, 2013: Airborne Radar Observations of Severe Hailstorms: Implications for Future Spaceborne Radar. *J. Appl. Meteor. Climatol.*, **52**, 1851–1867.

Hou, A. Y., R. K. Kakar, S. Neeck, A. A. Azarbarzin, C. D. Kummerow, M. Kojima, R. Oki, K. Nakamura, and T. Iguchi, 2014: The Global Precipitation Measurement Mission. *Bull. Amer. Meteor. Soc.*, **95**, 701–722.

Houze Jr, R. A. and Coauthors, 2017: The Olympic Mountains Experiment (OLYMPEX)." *Bull. Amer. Meteor. Soc.*, doi: https://doi.org/10.1175/BAMS-D-16-0182.1

Intrieri, J. M., M. D. Shupe, T. Uttal, and B. J. McCarty, 2002: An annual cycle of Arctic cloud characteristics observed by radar and lidar at SHEBA. *J. Geophys. Res.*, 107, 8030, doi:10.1029/2000JC000423.

Jensen, M. P. and Coauthors, 2016: The Midlatitude Continental Convective Clouds Experiment (MC3E). *Bull. Amer. Meteor. Soc.*, doi: http://dx.doi.org/10.1175/BAMS-D-14-00228.1.

Jiang, J. H. and Coauthors, 2012: Evaluation of cloud and water vapor simulations in CMIP5 climate models using NASA “A-Train” satellite observations, *J. Geophys. Res.*, **117**(D14), D14105, doi: 10.1029/2011JD017237.

Johnson, R. H., T. M. Rickenbach, S. A. Rutledge, P. E. Ciesielski, and W. H. Schubert, 1999: Trimodal characteristics of tropical convection, *J. Climate*, **12**, 2397-2418.

Klein, S. A. and Coauthors, 2009: Intercomparison of model simulations of mixed-phase clouds observed during the ARM Mixed-Phase Arctic Cloud Experiment. I: Single-layer cloud. *Quart. J. Roy. Meteor. Soc.*, **135**, 979-1002.

Koeppe, C. E. and G. C. De Long, 1958: Weather and Climate. McGraw-Hill Book Company, Inc., 341pp.

Kummerow, C., 1993: On the accuracy of the Eddington approximation for radiative transfer in the microwave frequencies. *J. Geophys. Res.*, **98**, 2757-2765.

Liu, G., 2004: Approximation of single scattering properties of ice and snow particles for high microwave frequencies. *J. Atmos. Sci.*, **61**, 2441-2456.

Liu, Y., W. P. Arnott and J. Hallett, 1998: Anomalous diffraction theory for arbitrarily oriented finite circular cylinders and Comparisons with exact T-matrix results. *Appl. Opt*, 37, 5019-5030.

Liu, Y., J. R. Key, S. A. Ackerman, G. G. Mace, and Q. Zhang, 2012: Arctic cloud macrophysical characteristics from CloudSat and CALIPSO. *Remote Sens. Env.*, **124**, 159-173.

Liou, K.-N., 1980: An Introduction to Atmospheric Radiation. Academic Press, 392pp.

Magono, C., and C. W. Lee, 1966: Meteorological Classification of Natural Snow Crystals. *J. Fac. Sci.*, Hokkaido Univ., **7**, 321-335.

Marchand, R., G. G. Mace, T. Ackerman and G. Stephens, 2008: Hydrometeor detection using CloudSat—An Earth-orbiting 94-GHz cloud radar. *J. Atmos. Oceanic Technol.*, **25**, 519–533.

Murray, B. J., C. G. Salzmann, A. J. Heymsfield, S. Dobbie, R. R. Neely III, and C. J. Cox, 2015: Trigonal Ice Crystals in Earth's Atmosphere. *Bull. Amer. Meteor. Soc.*, **96**, 1519–1531.

Neely III, R. R., M. Hayman, R. Stillwell, J. P. Thayer, R. M. Hardesty, M. O'Neill, M. D. Shupe, and C. Alvarez, 2013: Polarization lidar at Summit, Greenland, for the detection of cloud phase and particle orientation. *J. Atmos. Oceanic Tech.*, **30**, 1635–1655.

Noel, V. and H. Chepfer, 2010: A global view of horizontally oriented crystals in ice clouds from Cloud-Aerosol Lidar and Infrared Pathfinder Satellite Observation (CALIPSO). *J. Geophys. Res.*, **115**, D00H23, doi:10.1029/2009JD012365.

Olson, W. S., P. Bauer, C. D. Kummerow, Y. Hong, W.-K. Tao, 2001a: A melting-layer model for passive/active microwave remote sensing applications. Part II: simulation of TRMM observations. *J. Appl. Meteor*., **40**, 1164-1179.

Olson, W. S., Y. Hong, C. D. Kummerow, and J. Turk, 2001b: A texture-polarization method for estimating convective-stratiform precipitation area coverage from passive microwave radiometer data. *J. Appl. Meteor*., **40**, 1577-1591.

Pruppacher, H. R. and J. D. Klett, 1997: *Microphysics of clouds and precipitation*. Kluwer, 954 pp.

Riehl, H. and J. S. Malkus, 1958: On the heat balance in the equatorial trough zone. *Geophysica*, **6**, 503–538.

Roach, W. T., 1976: On the effect of radiative exchange on the growth by the condensation of a cloud or fog droplet. *Quart. J. Roy. Meteor. Soc.*, **102**, 361-372.

Roberti, L., and C. Kummerow, 1999: Monte Carlo calculations of polarized microwave radiation emerging from cloud structures. *J. Geophys. Res.*, **104**(D2), 2093–2104.

Rogers R. R. and M. K. Yau, 1989: *A short course in cloud physics*. 3rd Edition, Butterworth-Heinemann, Oxford. 290pp.

Sassen, K., 1974: Depolarization of laser light backscattered by artificial ice clouds. *J. Appl. Meteor.*, **13**, 923–933.

Shupe, M. D., D. D. Turner, V. P. Walden, R. Bennartz, M. Cadeddu, B. Castellani, C. Cox, D. Hudak, M. Kulie, N. Miller, R. R. Neely III, W. Neff, and P. Rowe, 2013: High and Dry: New observations of tropospheric and cloud properties above the Greenland Ice Sheet. *Bull. Amer. Meteor. Soc.*, **94**, 169-186.

Skofronick-Jackson, G., A. Heymsfield, E. Holthaus, C. Albers, and M.-J. Kim (2008), Nonspherical and spherical characterization of ice in Hurricane Erin for wideband passive microwave comparisons. *J. Geophys. Res.*, **113**, D06201, doi:10.1029/2007JD008866.

Skofronick-Jackson, G. and B. T. Johnson, 2011: Surface and atmospheric contributions to passive microwave brightness temperatures for falling snow events. *J. Geophys. Res.*, **116**, D02213, doi:10.1029/2010JD014438.

Skofronick-Jackson, G. and Coauthors, 2015: Global Precipitation Measurement Cold Season Precipitation Experiment (GCPEX): For Measurement's Sake, Let It Snow. *Bull. Amer. Meteor. Soc.*, **96**, 1719–1741.

Starr, D. O., and M. Quante, 2002: Dynamical processes in cirrus clouds. *Cirrus*, Lynch, D. K., K. Sassen, D. O'C. Starr and G. Stephens Ed., Oxford University Press, New York. 256-264.

Stephens, G. L., 1983: The influence of radiative transfer on the mass and heat budgets of ice crystals falling in the atmosphere. *J. Atmos. Sci.*, **40**, 1729-1739.

Stephens, G. L., D. G. Vane, R. J. Boain, G. G. Mace, K. Sassen, Z. Wang, A. J. Illingworth, E. J. O'Connor, W. B. Rossow, S. L. Durden, S. D. Miller, R. T. Austin, A. Benedetti, C. Mitrescu, and the CloudSat Science Team, 2002: The CloudSat mission and the A-TRAIN: A new dimension to space-based observations of clouds and precipitation. *Bull. Am. Met. Soc.*, **83**, 1771-1790.

Wang, J. R., P. E. Racette, J. E. Piepmeier, B. Monosmith, and W. Manning, 2007: Airborne CoSMIR observations between 50 and 183 GHz over snow-covered Sierra Mountains. *IEEE Trans. Geosci. Remote Sens.*, **45**, 55-61.

Wang, J. R., P. E. Racette, and J. R. Piepmeier, 2008: A comparison of near concurrent measurements from the SSMIS and CoSMIR for some selected channels over the frequency range of 50-183 GHz. *IEEE Trans. Geosci. Remote Sens.*, **46**, 923-933.

Webster, P. J. and G. L. Stephens, 1980: Tropical upper-tropospheric extended clouds: Inferences from Winter MONEX. *J. Atmos. Sci.,* **37,** 1521-1541.

Wu, T., W. R. Cotton, and W. Y. Y. Cheng, 2000: Radiative effects on the diffusional growth of ice particles in cirrus clouds. *J. Atmos. Sci.*, **57**, 2892-2904.

Yang, P., H. Wei, H.-L. Huang, B. A. Baum, Y. X. Hu, G. W. Kattawar, M. I. Mishchenko, and Q. Fu, 2005: Scattering and absorption property database for nonspherical ice particles in the near- through far-infrared spectral region. *App. Optics*, **44**, 5512-5523.

Zeng, X., 2008: The influence of radiation on ice crystal spectrum in the upper troposphere. *Quart. J. Roy. Meteor. Soc.*, **134**, 609-620.

Zeng, X., W.-K. Tao, M. Zhang, A. Y. Hou, S. Xie, S. Lang, X. Li, D. Starr, and X. Li, 2009: A contribution by ice nuclei to global warming. *Quart. J. Roy. Meteor. Soc.*, **135**, 1614-1629.

Zeng, X., G. Skofronick-Jackson, L. Tian, A. E. Emory, W. S. Olson and R. A. Kroodsma, 2016: Analysis of the GMI/CoSMIR microwave polarization data for ice crystal modeling. The 2016 Precipitation Measurement Mission (PMM) meeting, Houston, Texas, Oct. 24-28, 2016.

Zhang, M. and Coauthors, 2005: Comparing clouds and their seasonal variations in 10 atmospheric general circulation models with satellite measurements. *J. Geophy. Res.*, **110**(D15), D15S02, doi: 10.1029/2004JD005021.

Zhou, C., P. Yang, A. E. Dessler, Y. Hu, and B. A. Baum, 2012: Study of horizontally oriented ice crystals with CALIPSO Observations and Comparison with Monte Carlo Radiative Transfer Simulations. *J. Appl. Meteor. Clim.*, **51**, 1426-1439.

Table 1 List of the Numerical Experiments

Experiment	Crystal Shape (orientation)	*w*	Notes
Ph	+ Plate (horizontal)	0	Default experiment
PhPv	+ Plate (horizontal) + Plate (vertical)	0	Selection of crystal orientation
ChCv	+ Column (horizontal) + Column (vertical)	0	
PhS	+ Plate (horizontal) + Spherical solid crystals	0	Selection of crystal shape
PhCh	+ Plate (horizontal) + Column (horizontal)	0	
PhPvW	+ Plate (horizontal) + Plate (vertical)	1 cm s^{-1}	Effect of vertical velocity

Caption

Figure 1 Schematic diagram of REM for two adjacent ice crystals. The saturation water vapor pressure around an ice crystal E_i varies with crystal size, where the red and green lines denote E_i with η >1 and η < 1, respectively. When η <1, water vapor pressure e is lower (or higher) than E_i of the smaller (or larger) crystal. As a result, the smaller crystal sublimates with the resulting water vapor depositing on and therefore increasing the larger crystal.

Figure 2 Schematic diagrams of horizontally (left) and vertically (right) oriented plate crystals that receive the upward (F^+), downward (F^-) and horizontal infrared radiation ($\sim\sigma T^4$). Since F^+ and F^- usually deviate from σT^4, the horizontally- and vertically-oriented crystals have different energy budgets and therefore different surface temperature.

Figure 3 Evolution of the mass density $dM(\ln a)/d\ln a$ versus the half crystal size a in Exp. Ph for the horizontally-oriented plate crystals at η_z = 0.5, T=-30°C and p=300 hpa. The thick line denotes the initial spectrum and the time interval between lines is 30 minutes.

Figure 4 Time series of the average crystal size (top), the ice water content (middle) and the relative humidity with respect to ice (bottom) in Exp. Ph.

Figure 5 Evolution of the mass density $dM(\ln a)/d\ln a$ versus the half crystal size a in Exp. PhPv for the vertically- (top) and horizontally-oriented (bottom) plate crystals. The thick lines denote the initial spectra and the time interval between lines is 30 minutes.

Figure 6 Same as Figure 5 except for Exp. ChCv on column crystals.

Figure 7 Average crystal size versus time in Exp. PhS. The thick and thin lines represent the average size of horizontally-oriented plate crystals and the average radius of spherical ice crystals, respectively.

Figure 8 Evolution of the horizontally-oriented plate crystals in Exp. PhPvW with a vertical velocity of 1 cm s^{-1}.

Figure 9 Time series of the average crystal size (top) and ice water content (bottom) in Exps. PhPv (solid) and PhPvW (dashed line). The thick and thin lines in the top panel represent the average sizes of horizontally- and vertically-oriented plate crystals, respectively.

Figure 10 Vertical profiles of the radiative ratio η_z in clear sky in the high latitudes during wintertime (thick) and summertime (thin line).

Figure 11 The radiative ratio η_z versus height in clear sky in the Tropics (red), middle latitudes (green) and the arctic regions during wintertime (black).

Figure 12 The horizontal cross-section of radar reflectivities at 10 cm wavelength from NPOL at 3 km altitude and 2234 UTC, 23 May 2011 during MC3E. The red line shows the ER-2 flight track from 2223 to 2241 UTC 23 May 2011, during which the CoSMIR data are analyzed.

Figure 13 The polarization difference ΔT_b at 165.5 GHz between vertical and horizontal polarization obtained from the CoSMIR conical scan at nadir (top) and the reflectivities from the HIWRAP Ku-band (2.8 cm wavelength) measurements (bottom panel) along the flight track shown in Fig. 12 during MC3E.

Figure 14 Microwave polarization observations of the CoSMIR conical scan at 165.5 GHz (red) and GMI at 166 GHz (blue) over the OLYMPEX region on December 3 (left) and 5 (right), 2015, where a symbol corresponds to a scan pixel. The three black lines, representing the polarization difference (PD) of 0, 10 and 20K, respectively, are used for scaling.

Figure 15 The vertical cross-section of the CloudSat radar reflectivity (bottom) and the GMI polarization difference ΔT_b (=166V-166H) along the same CloudSat track (top) when both CloudSat and GPM flew over the Amazon. This dataset starts over 7.38S and 63.35W at 18:05:45 and end over 7.6N and 66.55W at 18:06:52 UTC 13 November 2014.

Figure 16 PDF of the GMI polarization difference ΔT_b at 166 GHz over land (left) and sea (right) in the Tropics. The blue, black, green and red lines represent atmospheric columns (or pixels) with the maximum radar reflectivity above 20 dBZ (deep convective clouds), between 5 and 20 dBZ (thick clouds), between -20 and 5 dBZ (thin clouds), and below -20 dBZ (clear sky and extremely thin clouds), respectively.

Figure 17 PDF of the GMI polarization difference ΔT_b at 166 GHz over land (top) and sea (bottom) versus latitude. The thick lines represent columns with the maximum radar reflectivity between 5 and 20 dBZ and the thin ones with the maximum radar reflectivity between -20 and 5 dBZ (referred to here as background) in the low (left), middle (middle) and high latitudes (right).

Figure 18 The fractions of thick clouds (left, with radar reflectivity between 5 and 20 dBZ) and thin clouds (right, between -20 and 5 dBZ) observed by CloudSat over the

Tropics. Their values are normalized by their total cloud pixel numbers above 2 km, respectively.

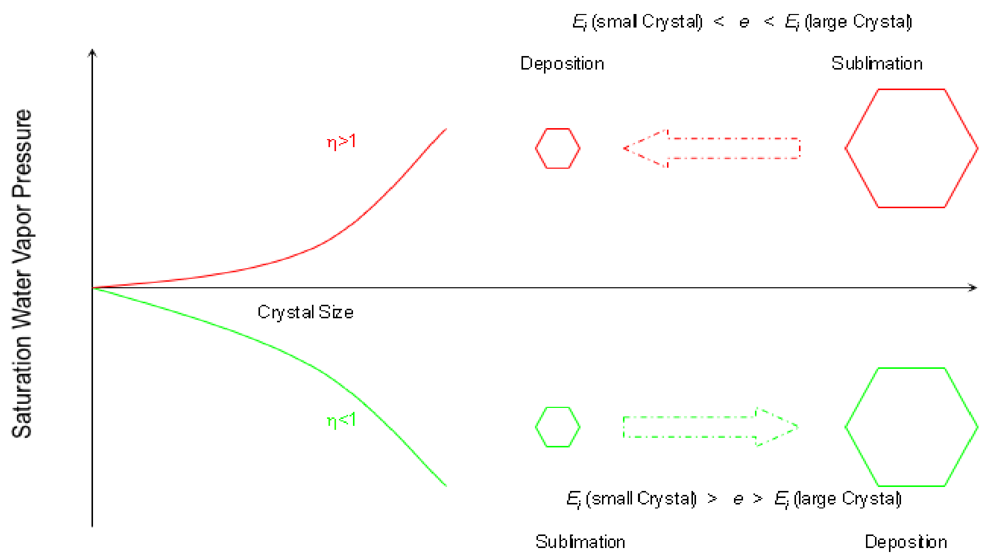

Figure 1 Schematic diagram of REM for two adjacent ice crystals. The saturation water vapor pressure around an ice crystal E_i varies with crystal size, where the red and green lines denote E_i with η >1 and η < 1, respectively. When η <1, water vapor pressure e is lower (or higher) than E_i of the smaller (or larger) crystal. As a result, the smaller crystal sublimates with the resulting water vapor depositing on and therefore increasing the larger crystal.

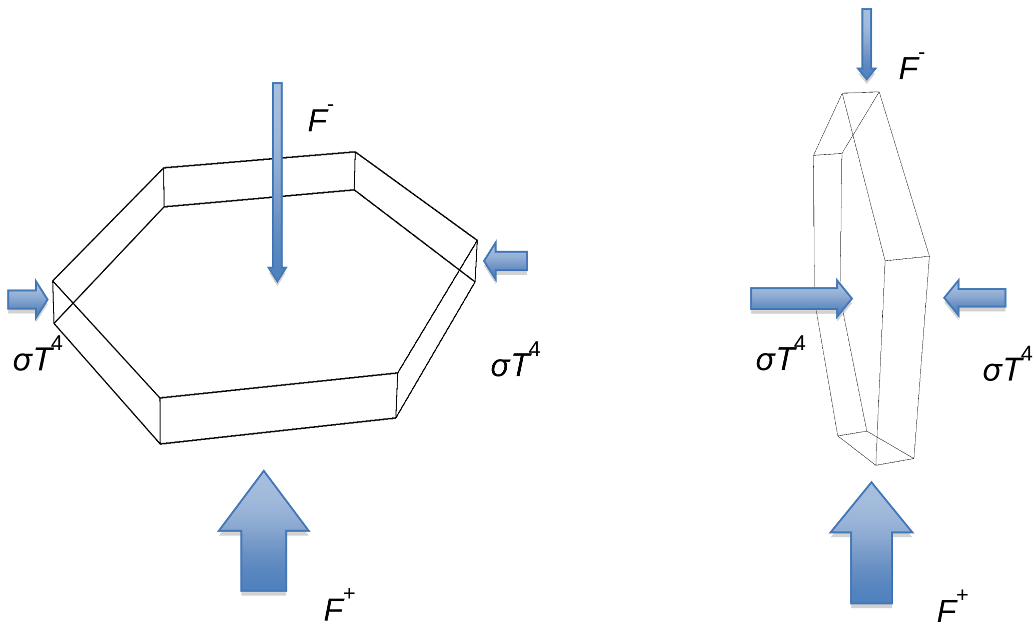

Figure 2 Schematic diagrams of horizontally (left) and vertically (right) oriented plate crystals that receive the upward (F^+), downward (F^-) and horizontal infrared radiation ($\sim\sigma T^4$). Since F^+ and F^- usually deviate from σT^4, the horizontally- and vertically-oriented crystals have different energy budgets and therefore different surface temperature.

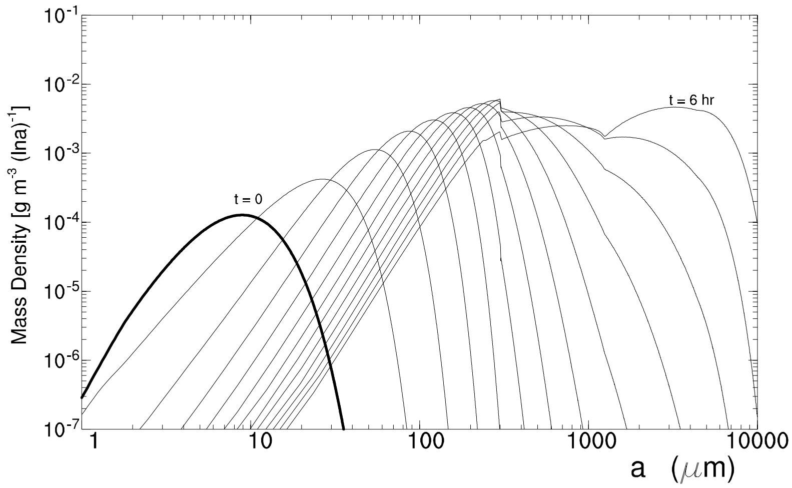

Figure 3 Evolution of the mass density $dM(\ln a)/d\ln a$ versus the half crystal size a in Exp. Ph for the horizontally-oriented plate crystals at η_z = 0.5, T=-30°C and p=300 hpa. The thick line denotes the initial spectrum and the time interval between lines is 30 minutes.

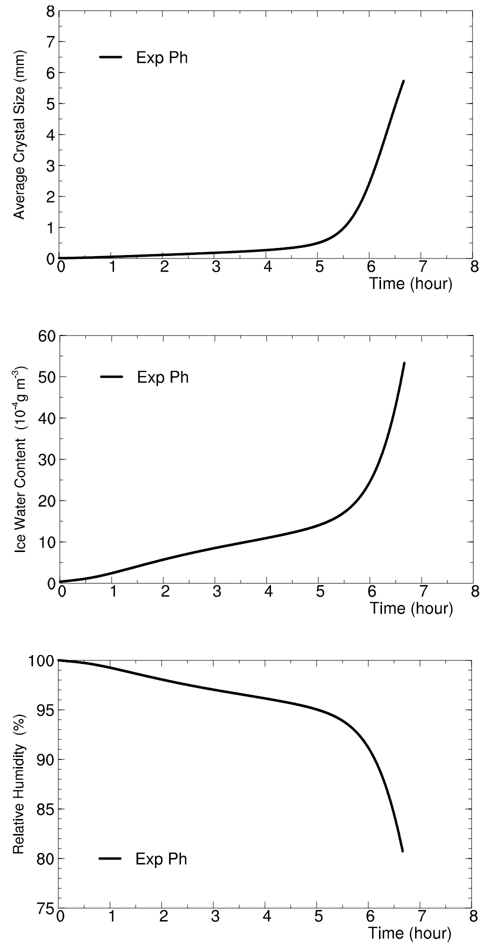

Figure 4 Time series of the average crystal size (top), the ice water content (middle) and the relative humidity with respect to ice (bottom) in Exp. Ph.

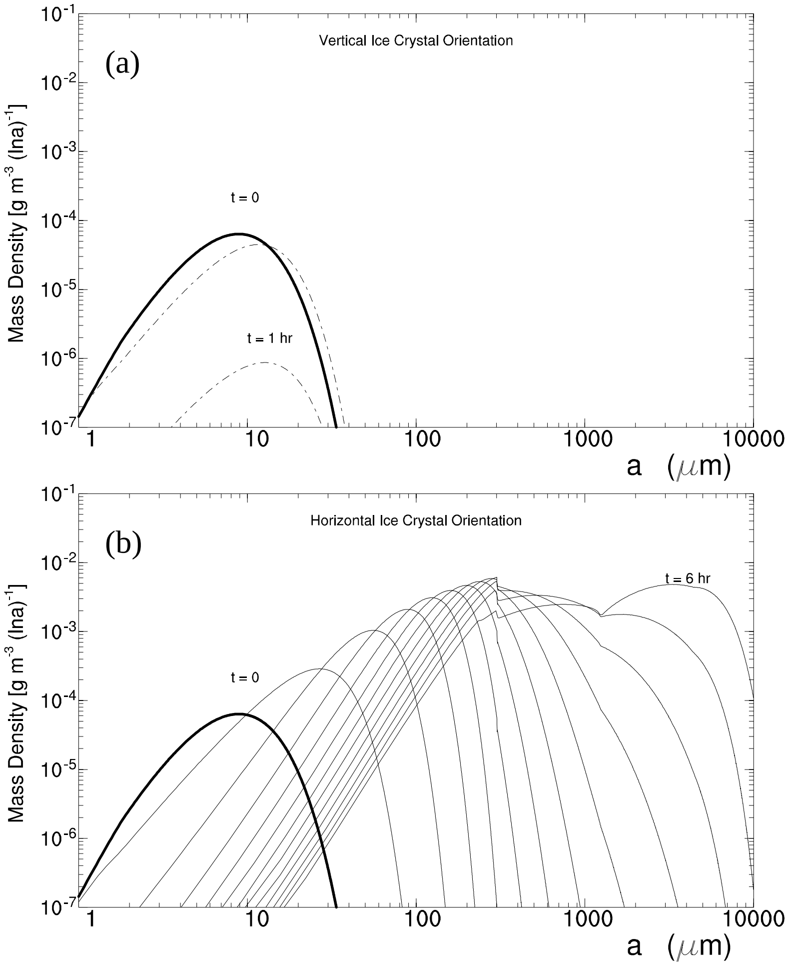

Figure 5 Evolution of the mass density $dM(\ln a)/d\ln a$ versus the half crystal size a in Exp. PhPv for the vertically- (top) and horizontally-oriented (bottom) plate crystals. The thick lines denote the initial spectra and the time interval between lines is 30 minutes.

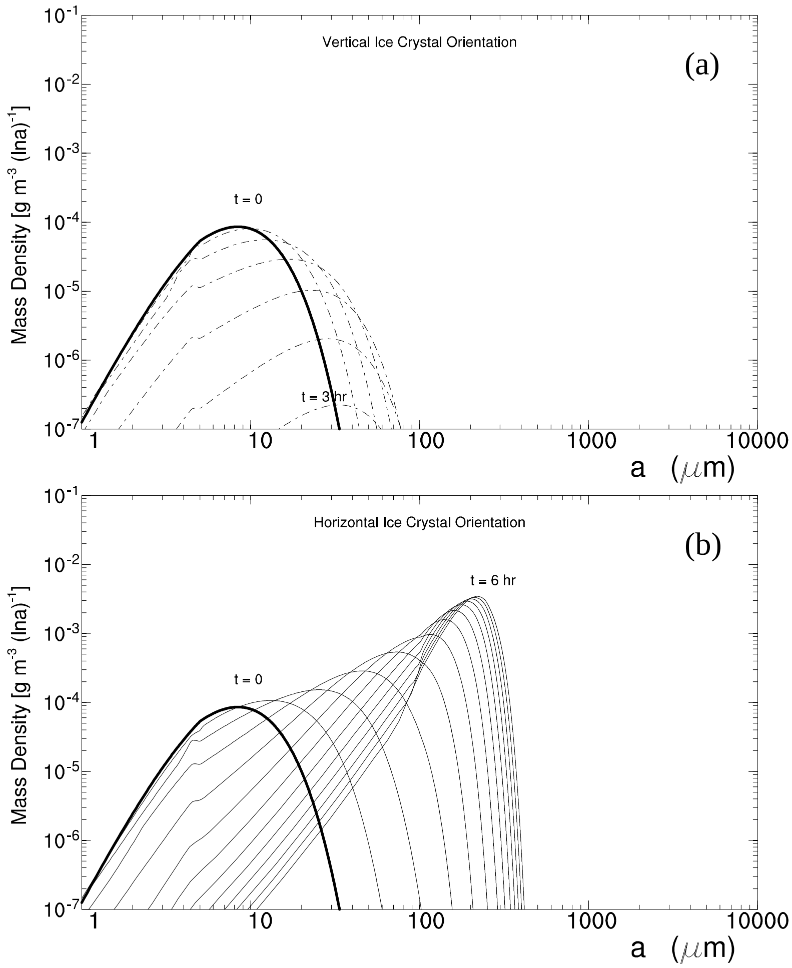

Figure 6 Same as Figure 5 except for Exp. ChCv on column crystals.

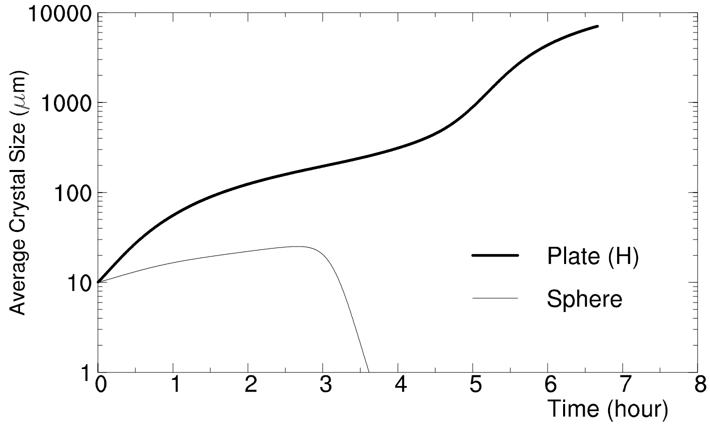

Figure 7 Average crystal size versus time in Exp. PhS. The thick and thin lines represent the average size of horizontally-oriented plate crystals and the average radius of spherical ice crystals, respectively.

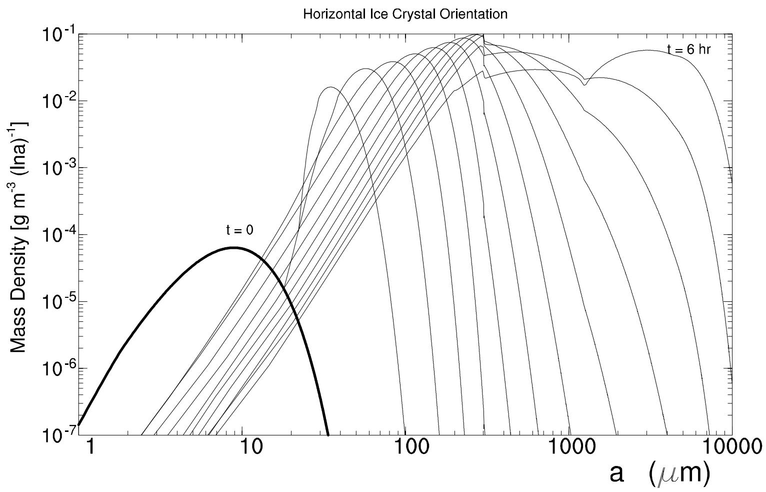

Figure 8 Evolution of the horizontally-oriented plate crystals in Exp. PhPvW with a vertical velocity of 1 cm s^{-1}.

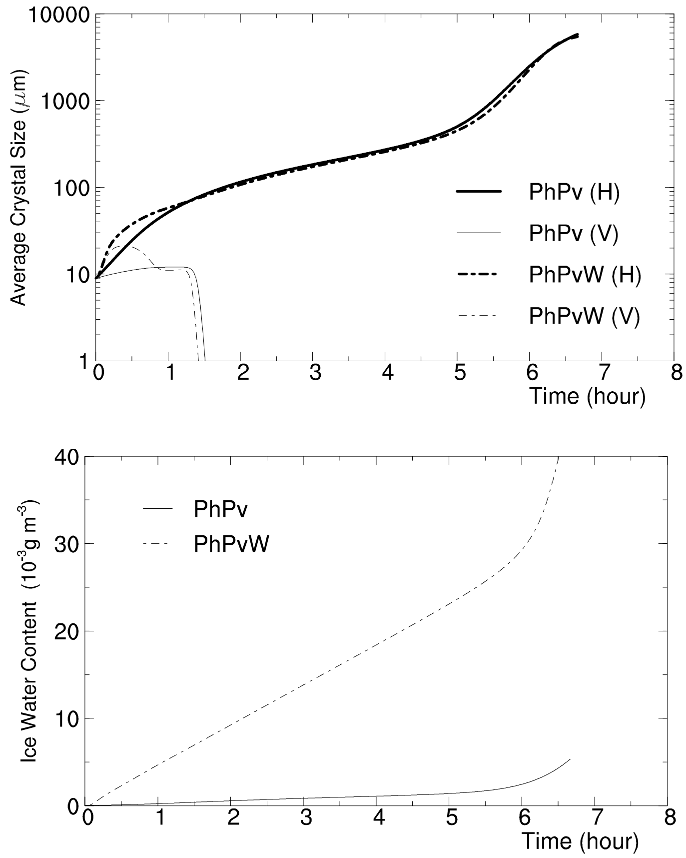

Figure 9 Time series of the average crystal size (top) and ice water content (bottom) in Exps. PhPv (solid) and PhPvW (dashed line). The thick and thin lines in the top panel represent the average sizes of horizontally- and vertically-oriented plate crystals, respectively.

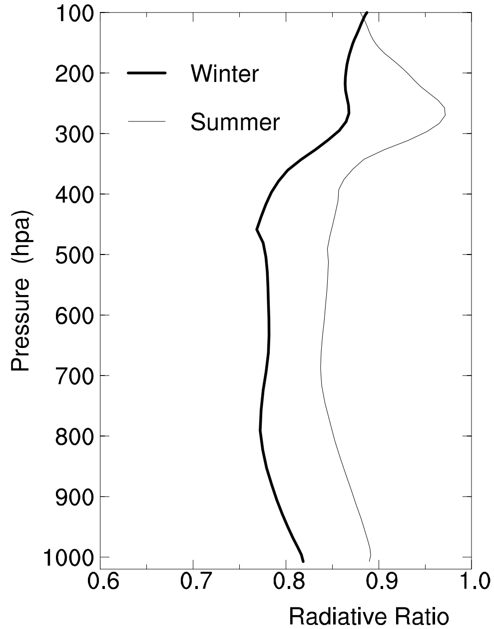

Figure 10 Vertical profiles of the radiative ratio η_z in clear sky in the high latitudes during wintertime (thick) and summertime (thin line).

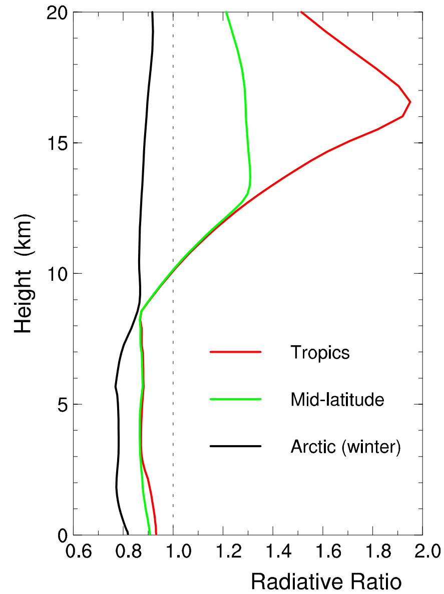

Figure 11 The radiative ratio η_z versus height in clear sky in the Tropics (red), middle latitudes (green) and the arctic regions during wintertime (black).

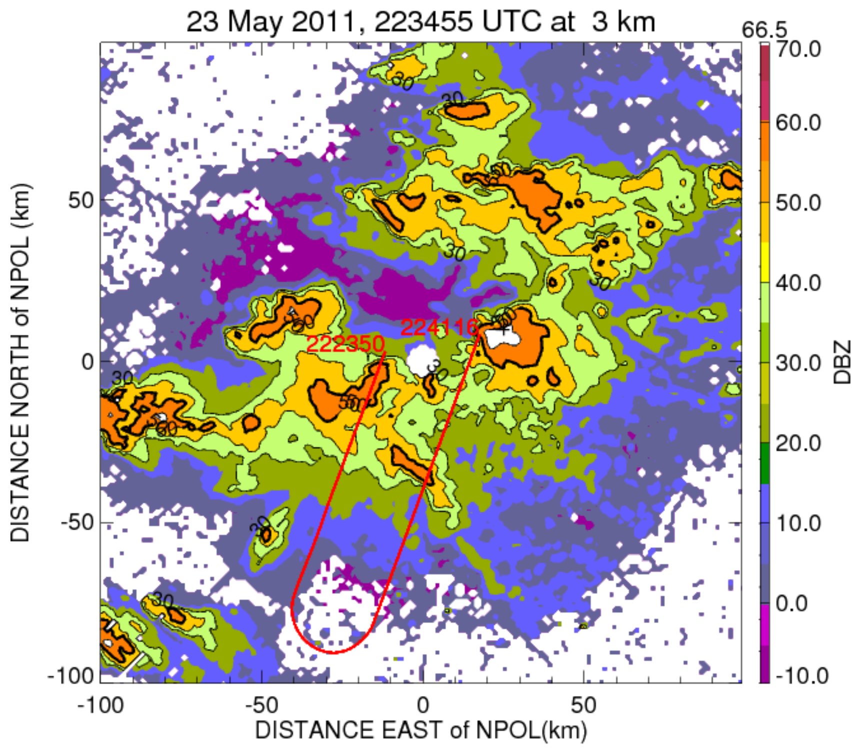

Figure 12 The horizontal cross-section of radar reflectivities at 10 cm wavelength from NPOL at 3 km altitude and 2234 UTC, 23 May 2011 during MC3E. The red line shows the ER-2 flight track from 2223 to 2241 UTC 23 May 2011, during which the CoSMIR data are analyzed.

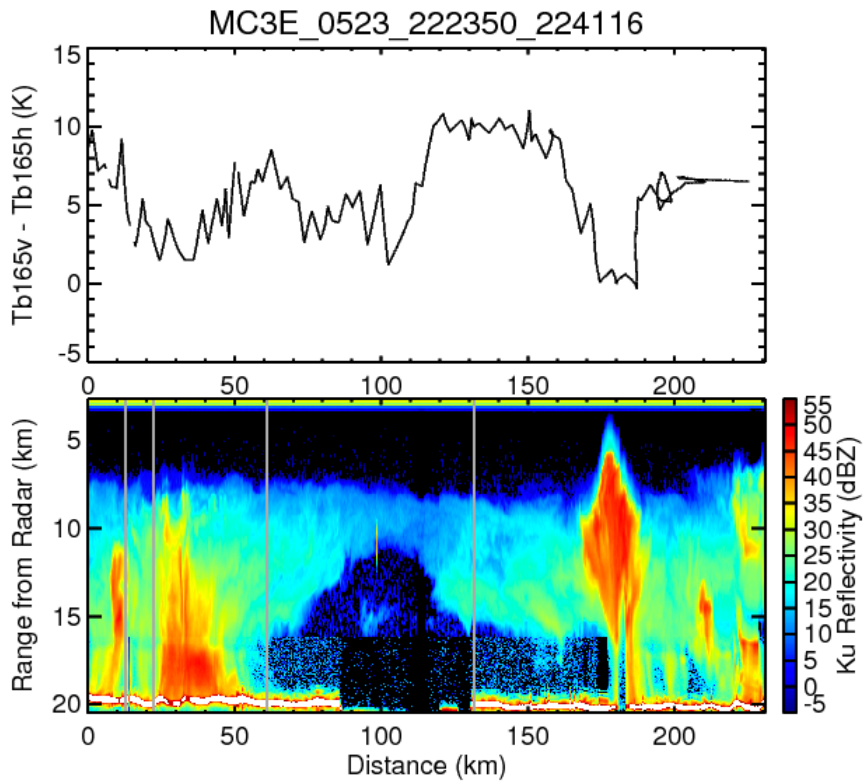

Figure 13 The polarization difference ΔT_b at 165.5 GHz between vertical and horizontal polarization obtained from the CoSMIR conical scan at nadir (top) and the reflectivities from the HIWRAP Ku-band (2.8 cm wavelength) measurements (bottom panel) along the flight track shown in Fig. 12 during MC3E.

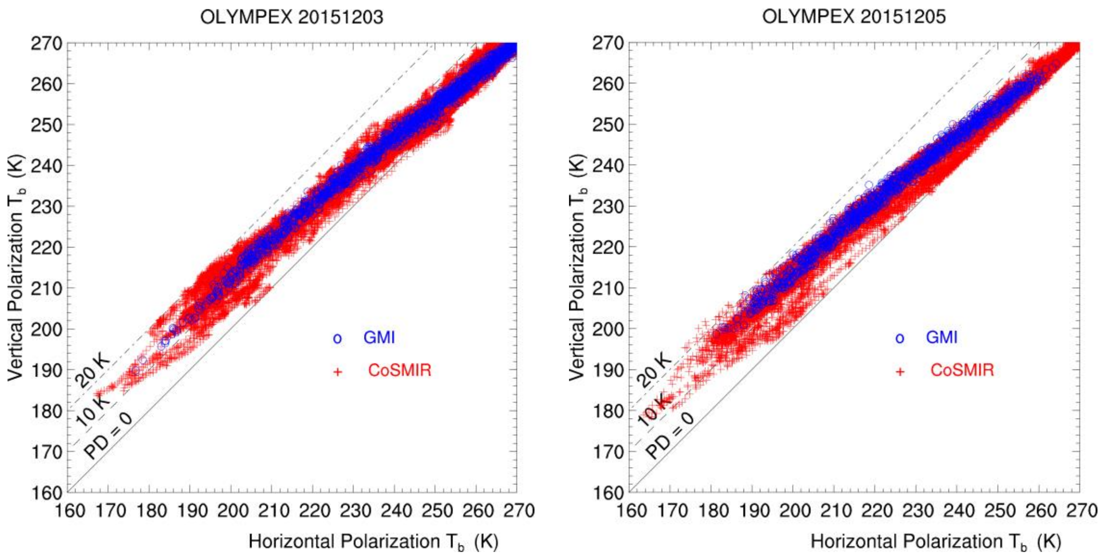

Figure 14 Microwave polarization observations of the CoSMIR conical scan at 165.5 GHz (red) and GMI at 166 GHz (blue) over the OLYMPEX region on December 3 (left) and 5 (right), 2015, where a symbol corresponds to a scan pixel. The three black lines, representing the polarization difference (PD) of 0, 10 and 20K, respectively, are used for scaling.

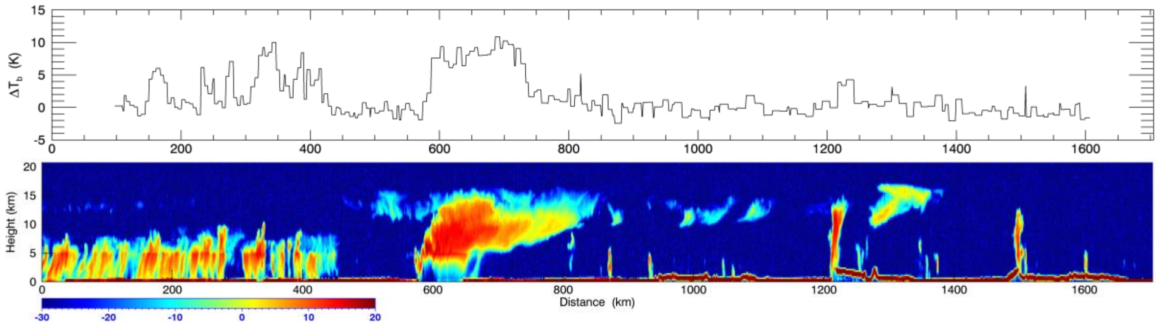

Figure 15 The vertical cross-section of the CloudSat radar reflectivity (bottom) and the GMI polarization difference ΔT_b (=166V-166H) along the same CloudSat track (top) when both CloudSat and GPM flew over the Amazon. This dataset starts over 7.38S and 63.35W at 18:05:45 and end over 7.6N and 66.55W at 18:06:52 UTC 13 November 2014.

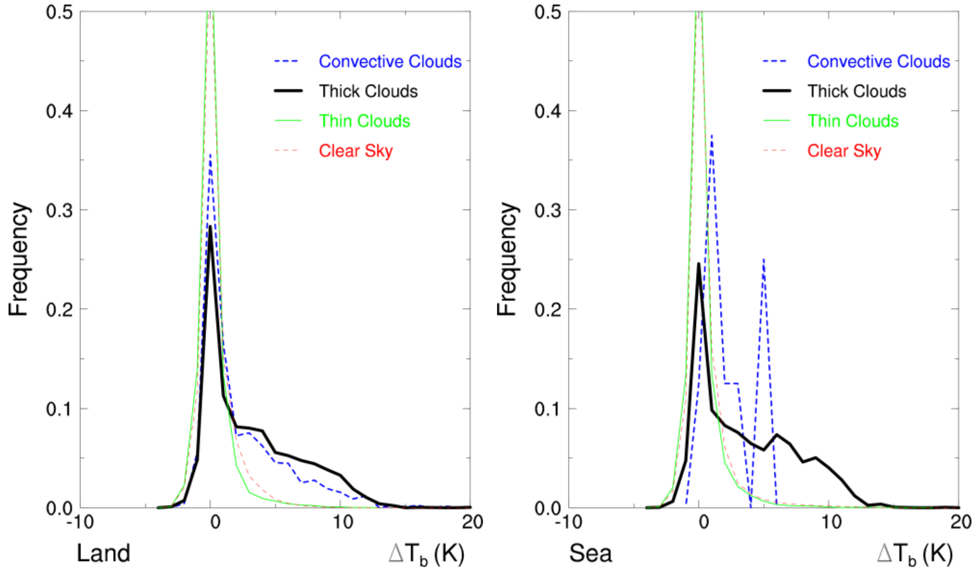

Figure 16 PDF of the GMI polarization difference ΔT_b at 166 GHz over land (left) and sea (right) in the Tropics. The blue, black, green and red lines represent atmospheric columns (or pixels) with the maximum radar reflectivity above 20 dBZ (deep convective clouds), between 5 and 20 dBZ (thick clouds), between -20 and 5 dBZ (thin clouds), and below -20 dBZ (clear sky and extremely thin clouds), respectively.

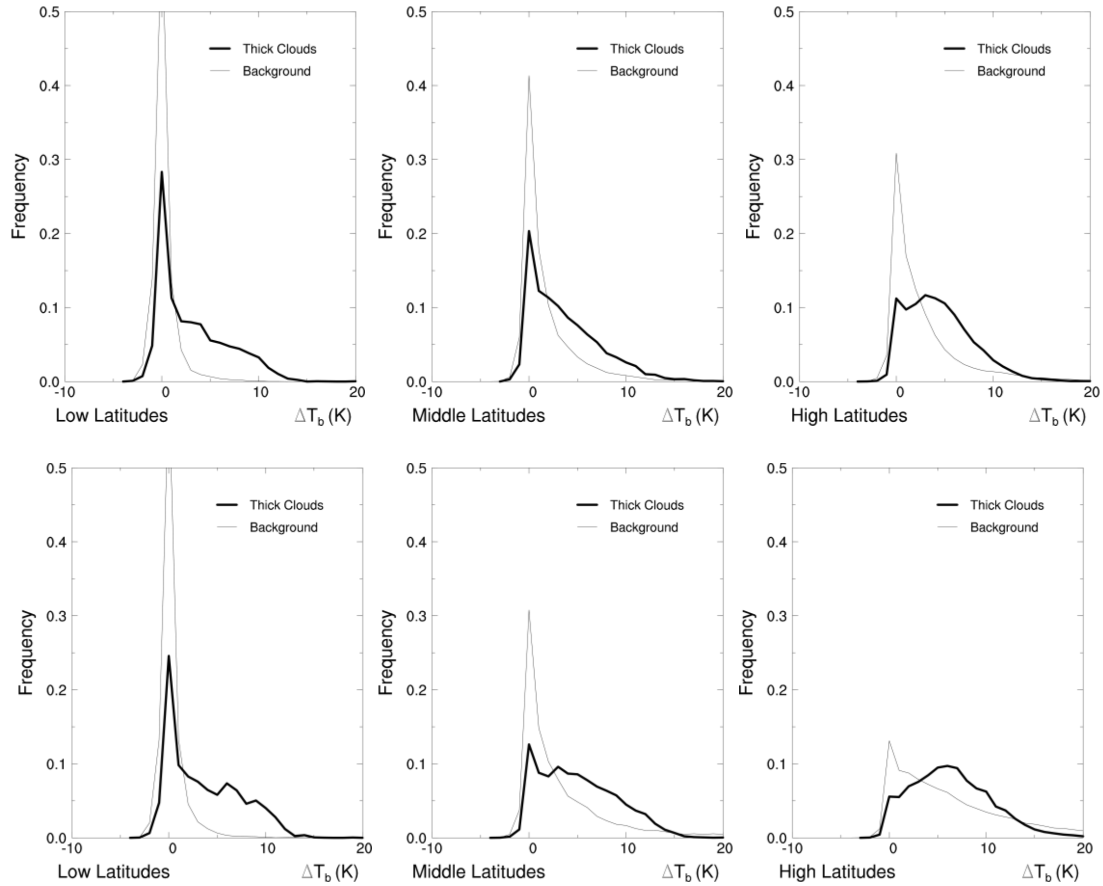

Figure 17 PDF of the GMI polarization difference ΔT_b at 166 GHz over land (top) and sea (bottom) versus latitude. The thick lines represent columns with the maximum radar reflectivity between 5 and 20 dBZ and the thin ones with the maximum radar reflectivity between -20 and 5 dBZ (referred to here as background) in the low (left), middle (middle) and high latitudes (right).

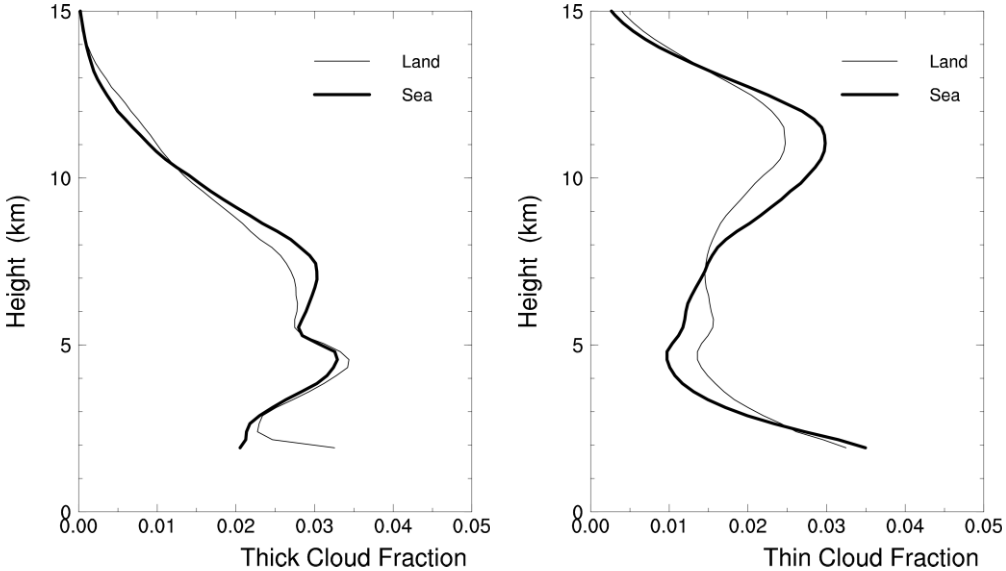

Figure 18 The fractions of thick clouds (left, with radar reflectivity between 5 and 20 dBZ) and thin clouds (right, between -20 and 5 dBZ) observed by CloudSat over the Tropics. Their values are normalized by their total cloud pixel numbers above 2 km, respectively.